

# Growth Kinetics of $\beta'$ Precipitation in a Ferritic Matrix During Isothermal Aging of Cu-containing Fe-10at.%Ni-15at.%Al alloys

Hector J. Dorantes-Rosales<sup>a</sup>, Carlos Ferreira-Palma<sup>b</sup> , Victor M. Lopez-Hirata<sup>a\*</sup> ,

Maribel L. Saucedo-Muñoz<sup>a</sup>, Erika O. Avila-Davila<sup>c</sup>, Felipe Hernandez-Santiago<sup>a</sup>,

José D. Villegas-Cárdenas<sup>a</sup> , Diego Rivas-Lopez<sup>a</sup>

<sup>a</sup>Instituto Politecnico Nacional, Cd. Mx. 07300, Mexico.

<sup>b</sup>Universidad Veracruzana, Centro de Investigación en Micro y Nanotecnología, Boca del Rio, Mexico.

<sup>c</sup>Instituto Tecnológico de Pachuca, Tecnológico Nacional de México, Hidalgo, Mexico.

Received: May 17, 2021; Revised: July 23, 2021; Accepted: August 15, 2021

A precipitation study was carried out during the isothermal aging at 850 °C for Fe-10at.%Ni-15at.%Al, Fe-10at.%Ni-15at.%Al-2.5at.%Cu and Fe-10at.%Ni-15at.%Al-5at.%Cu alloys. The experimental, Calphad, and Kinetic/Precipitation calculated results indicated that the Cu-addition to the ternary alloy promoted a higher volume fraction of  $\beta'$  precipitates, which caused a better aging response for the Cu-containing alloys. The coarsening resistance was the highest for the 2.5 at. % Cu-containing alloy, compared to the ternary alloy because of its lower interfacial free energy, 0.009 Jm<sup>-2</sup>, between the precipitate and the matrix. The Cu alloying element was located mainly in the  $\beta'$  precipitate according to its expected thermodynamic behavior, and it caused an atomic relation of Ni to Al close to that of NiAl intermetallic compound for the  $\beta'$  phase. A content of 5 at. % Cu in the ternary alloy promoted higher interfacial energy, 0.04 Jm<sup>-2</sup>, and thus the fastest coarsening process.

**Keywords:** Fe-Ni-Al base alloys, Cu addition,  $\beta'$  precipitation, growth kinetics, numerical simulation, aging response.

## 1. Introduction

The development of heat-resistant alloys is a critical issue to satisfy the current requirements of industrial equipment used in the power generation and petrochemical industries<sup>1</sup>. Most of these alloys based their mechanical strength and creep properties on the precipitation of different phases in a soft matrix. These precipitates include, for instance, M<sub>23</sub>C<sub>6</sub>, M<sub>7</sub>C<sub>3</sub>, MC carbides,  $\eta$  phase, Ni<sub>3</sub>Al  $\gamma$ , and NiAl  $\beta'$  phase used in both ferrous and nonferrous alloys<sup>1,2</sup>. The size, distribution, morphology, and coherence play a significant role to keep their creep strength during service operation at high temperatures<sup>1-4</sup>. The study of Fe-Ni-Al based alloys can contribute to developing diverse engineering alloys such as PH stainless steels and Fe-Cr-Ni-Al alloys. The coherent precipitation of  $\beta'$  phase in a  $\alpha$  ferrite matrix phase is responsible for the creep strength after aging treatment during the service operation. The NiAl-type  $\beta'$  phase has a B2 (CsCl) crystalline structure<sup>3</sup>. Additional advantages of Fe-Ni-Al alloys are their lower density and cost than that of Ni-based superalloys<sup>5,6</sup>.

The precipitate coarsening or Ostwald ripening is a common metallurgical phenomenon, which takes place in industrial components at high temperatures. This fact causes a decrease in the mechanical properties because of the formation of large precipitates, and the dissolution of small precipitates

during the aging process<sup>7-13</sup>. The mechanical properties of alloys at high temperatures can be maintained by increasing the coarsening resistance of precipitates. This increase can be obtained either by decreasing the interfacial free energy between the interface of precipitate and the matrix, the solute solubility, or the atomic diffusion in the matrix phase<sup>14-17</sup>. Thus, the use of alloying elements is a possible alternative to decrease the coarsening growth since it strongly affects these parameters. For instance, the addition of Cu to the ternary Fe-Ni-Al alloys is expected to have a decreasing effect on the ferrite solubility since Cu is well known to exhibit poor solubility in bcc ferrite. In contrast, it is quite soluble in Ni, and it presents more than 4 at. % solubility in Al<sup>14</sup>. The Cu addition may also affect the interfacial energy between the interface of precipitate and matrix. Therefore, the addition of Cu to this alloy system could modify the behavior of the coarsening growth kinetics of  $\beta'$  precipitates in a ferritic matrix<sup>14,15</sup>.

The Calphad and Precipitation/Kinetics software has been applied<sup>18-22</sup> successfully to analyze the precipitation process of different multicomponent alloy systems. Calphad permits to obtain the phase stability, interfacial free energy, driving force, coarsening rate constant, Time-Temperature-Precipitation diagrams, growth kinetics of precipitation, size distribution, change of yield strength after aging, etc. The above-calculated parameters can be used to analyze more precisely the  $\beta'$  precipitation of

\*e-mail: vlopezhi@prodigy.net.mx

Fe-Ni-Al based alloys, as well as the effect of alloying elements on both growth kinetics of precipitation and coarsening.

Therefore, this work aims to analyze numerically and experimentally the growth kinetics of precipitation and coarsening processes of  $\beta'$  precipitates in an  $\alpha$  ferritic matrix for the Fe-10at.%Ni-15at.%Al, Fe-10at.%Ni-15at.%Al-2.5at.%Cu and Fe-10at.%Ni-15at.%Al-5at.%Cu alloys during aging at 850 °C, as well as to know its effect on the aging response.

## 2. Numerical Methodology

The analysis of phase stability was conducted using Calphad software along with the thermodynamic and diffusion database for Fe-based alloys<sup>21</sup>. The chemical composition of alloys and temperature are usually specified to simulate with Calphad. Additionally, Precipitation/Kinetics software<sup>18,20,21</sup> was employed to simulate the  $\beta'$  precipitation in the ferritic  $\alpha$  phase matrix. It was considered the bulk nucleation of cuboid  $\beta'$  precipitates in the ferritic matrix and taking into account the effect of the elastic strain in the matrix.

## 3. Experimental Methodology

The following alloy compositions, Fe-10at.%Ni-15at.%Al, Fe-10at.%Ni-15at.%Al-2.5at.%Cu and Fe-10at.%Ni-15at.%Al-5at.%Cu, were vacuum melted using high purity Fe (99.9%), Ni (99.99%), Al (99.7%), and Cu (99.99%) elements with an electric-arc furnace under a pure argon atmosphere. The alloy chemical composition was verified using a Flame-Atomic Absorption Spectrometer. The actual composition was determined to be very close to the nominal one. The ingots were homogenized at 1100 °C for one week to eliminate the dendritic microstructure and make a uniform chemical composition. Specimens of 30 mm x 30 mm x 10 mm were cut and encapsulated in a quartz tube, under a pure argon atmosphere. The solution treatment was carried out at 1100 °C for 1 h, subsequently air-cooled, and aged at 850 °C for 5 to 150 h. All heat-treated specimens were metallographically prepared and then etched at room temperature with an etchant prepared with 15 ml hydrochloric acid, 10 ml nitric acid, and 10 ml acetic acid. These were subsequently observed with a conventional and Cold Field Emission Gun scanning electron microscope (FEG-SEM) using SEI technique at 25 kV, equipped with an energy dispersive X-ray spectrometer (EDX). The equivalent radius  $r$  of precipitates was measured by the precipitate area on SEM micrographs with an image analyzing system. The size measurements of precipitates mainly corresponded to those with cuboid morphology. Transmission Electron Microscope (TEM) specimens were also prepared by a two-jet electropolishing method with an electrolyte composed of 40 vol. % nitric acid in methanol at -60 °C and 20 V (d.c.), and subsequently observed by TEM at 200 kV. The Vickers hardness, HV 0.1 kg/12 s, was determined in all heat-treated specimens.

## 4. Results and Discussion

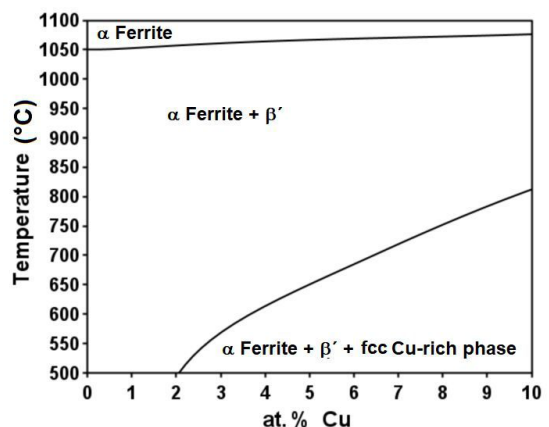
### 4.1. Thermodynamic stability of phases

The Calphad calculated equilibrium pseudobinary Fe-Cu phase diagram is shown in Figure 1 for the

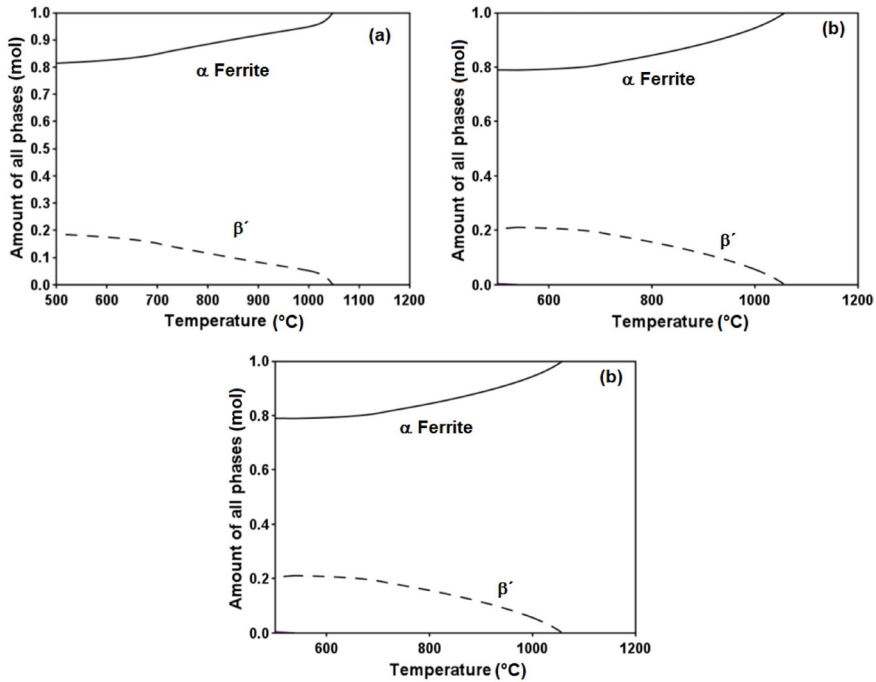
Fe-10at.%Ni-15at.%Al-5at.%Cu alloy. This diagram indicates mainly the presence of the  $\alpha$  ferrite,  $\beta'$  and fcc Cu-rich phases. The phase field of  $\alpha$  ferrite is stable at temperatures higher than approximately 1050 °C, and it becomes less stable as the Cu content increases. Thus, a temperature of about 1100 °C for the solution treatment is quite acceptable for Fe-10at.%Ni-15at.%Al alloys with a Cu content up to 10 at. %. As the temperature decreases, the  $\alpha$  ferrite and  $\beta'$  phases are present; however, the presence of a three-phase field,  $\alpha$  ferrite,  $\beta'$  and Cu-rich fcc phases is favored with the decrease in temperature and the increase in Cu content. The Calphad calculated plot for the amount of all phases in equilibrium as a function of temperature is present in Figure 2a-c for the Fe-10at.%Ni-15at.%Al Fe-10at.%Ni-15at.%Al-2.5at.%Cu and Fe-10at.%Ni-15at.%Al-5at.%Cu alloys, respectively. These figures indicate that the  $\alpha$  ferrite phase is stable at temperatures higher than approximately 1050 °C for the three alloy compositions. It can also be noted that the following precipitation reaction may occur at temperatures lower than approximately 1050 °C:



Figure 2a-c also indicate clearly that the  $\beta'$  phase precipitation increases with the decrease in temperature and the increase in Cu content. It is important to note that the precipitation of fcc Cu-rich phase can be present at aging temperatures lower than 600 °C for both Cu-containing alloys. This fact is more clearly shown in Figure 2c. An interesting point is that the volume fraction of  $\beta'$  phase has a maximum at a temperature of about 650 °C, which is more notorious as the Cu content increases. This characteristic may be attributable to the dissolution of the fcc Cu-rich phase, which is formed at lower temperatures. Figures 3 and 4a-c show the Calphad calculated chemical composition of the equilibrium  $\alpha$  ferrite and  $\beta'$  phases, respectively, for the three alloys previously described. The increase in the solubility of Ni, Al and Cu solutes with temperature in the  $\alpha$  ferrite phase is evident in these figures. Nevertheless, the Cu solubility in ferrite is very low, as expected for the binary Fe-Cu alloy system<sup>23</sup>. In contrast,



**Figure 1.** Calphad calculated equilibrium pseudobinary Fe-Cu phase diagram for Fe-10at.%Ni-15at.%Al-5at.%Cu alloy.



**Figure 2.** Calphad calculated plot of amount of all equilibrium phases versus temperature for (a) Fe-10at.%Ni-15at.%Al, (b) Fe-10at.%Ni-15at.%Al-2.5at.%Cu and (c) Fe-10at.%Ni-15at.%Al-5at.%Cu alloys.

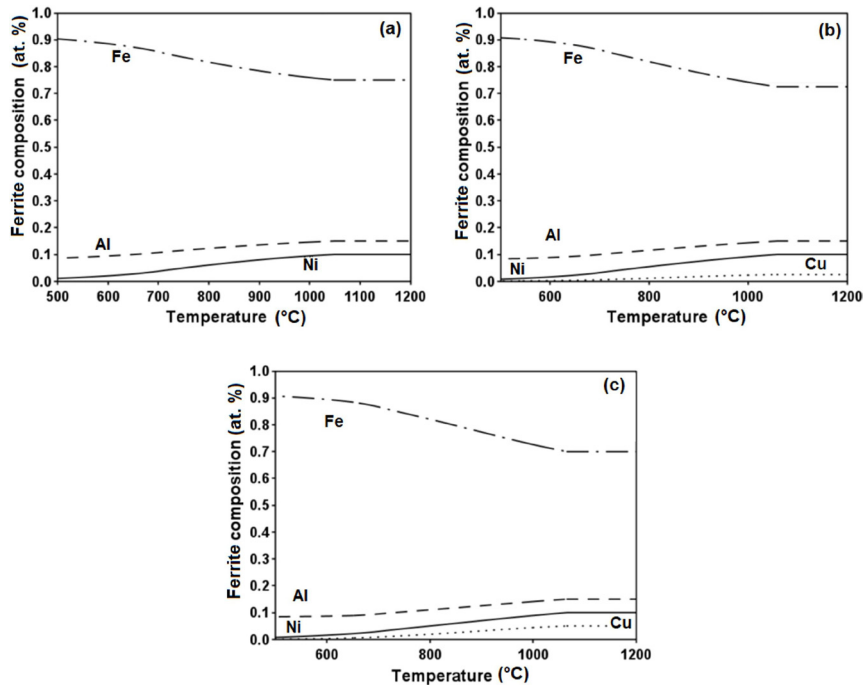


**Figure 3.** Plot of Calphad calculated chemical composition of the  $\alpha$  ferrite phase versus temperature for (a) Fe-10at.%Ni-15at.%Al, (b) Fe-10at.%Ni-15at.%Al-2.5at.%Cu and (c) Fe-10at.%Ni-15at.%Al-5at.%Cu alloys.

the amount of Ni and Al presents in the  $\beta'$  phase, being that of Ni higher, decreases with the increase in temperature, while that of Fe indicates an increase with temperature, Figure 4a-c. Besides, the Al content becomes higher than that of Ni at

temperatures above 900 °C. It is important to note that the mole fraction of Ni and Al at 500 °C becomes close to that of the NiAl intermetallic compound. Likewise, the Cu solubility increases in the  $\beta'$  phase, up to approximately 20 at. % at

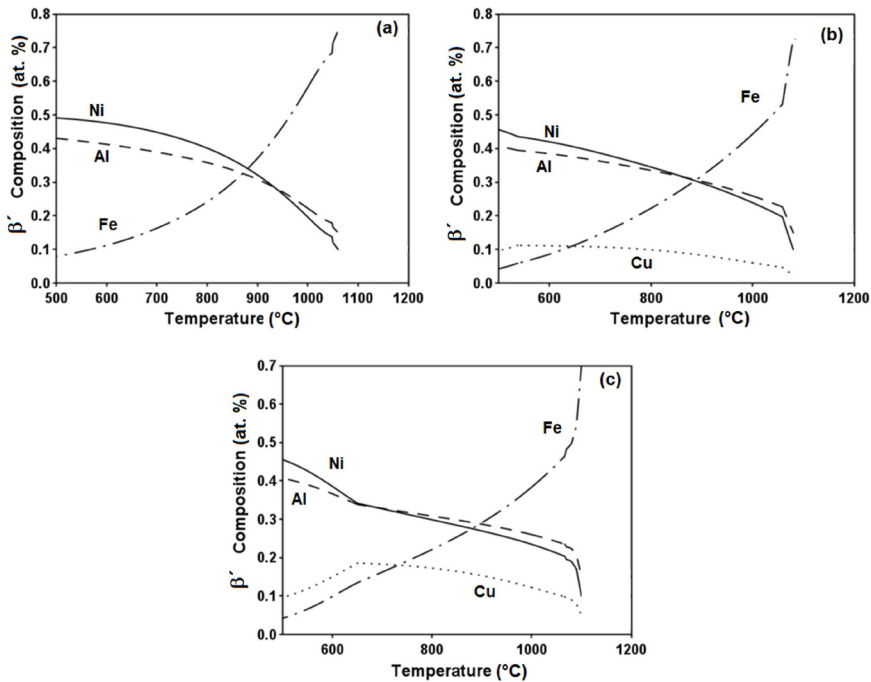


**Figure 4.** Plot of Calphad calculated chemical composition of the  $\beta'$  phase versus temperature for (a) Fe-10at.%Ni-15at.%Al, (b) Fe-10at.%Ni-15at.%Al-2.5at.%Cu and (c) Fe-10at.%Ni-15at.%Al-5at.%Cu alloys.

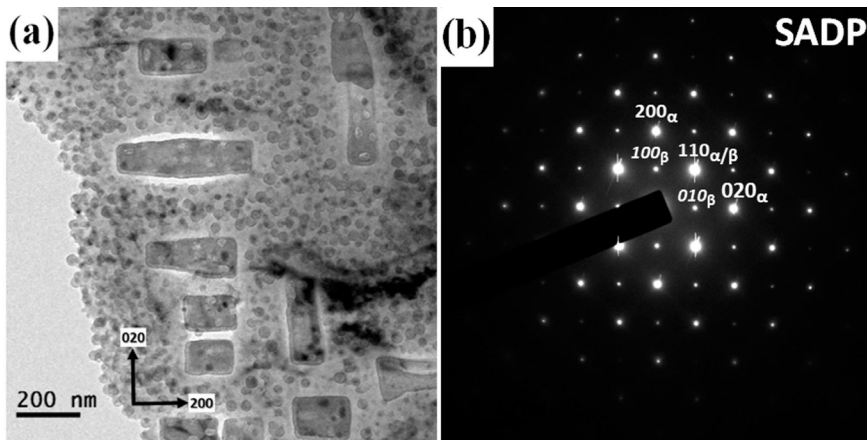


**Figure 5.** (a) BF-TEM micrograph of the Fe-10at.%Ni-15at.%Al-5at.%Cu alloy aged at 850 °C for 5 h, and (b) its corresponding SADP.

approximately 650 °C for the 5 at. % Cu-containing alloy, Figure 4c; however, it diminishes slightly at temperatures higher than 700 °C. This increase seems to be also related to the dissolution of the fcc Cu-rich phase<sup>24</sup>.

#### 4.2. Microstructure characterization

Figure 5a shows the Bright-Field BF-TEM micrograph of the Fe-10at.%Ni-15at.%Al-5at.%Cu alloy after aging at 850 °C for 5 h. Plate and cuboid  $\beta'$  precipitates can be observed in the  $\alpha$  ferrite matrix. The small spheroid precipitates of  $\beta'$  phase were formed during cooling of the aged specimen. The selected area electron diffraction pattern SADP of this TEM micrograph is shown in Figure 5b. This diffraction pattern corresponds to a zone axis [001] of the

bcc ferrite phase. The  $\beta'$  phase reflections are also between those of the ferrite matrix in the SADP of Figure 5b, and they correspond to a NiAl-type superlattice<sup>14,15</sup>. Additionally, the  $\beta'$  precipitates exhibit preferential alignment along the  $\langle 100 \rangle$  crystallographic direction of the ferrite matrix, which can be attributed to the fact that this direction presents a low value of the Young modulus for the bcc crystalline structure<sup>14</sup>.

FEG-SEM micrographs of the precipitation evolution are shown in Figures 6, 7 and 8a-d for the Fe-10at.%Ni-15at.%Al, Fe-10at.%Ni-15at.%Al-2.5at.%Cu and Fe-10at.%Ni-15at.%Al-5at.%Cu alloys, respectively, aged at 850 °C for different times. It is important to mention that fine primary precipitation was noted after air-cooling of the solution treatment for the alloys. In the case of the

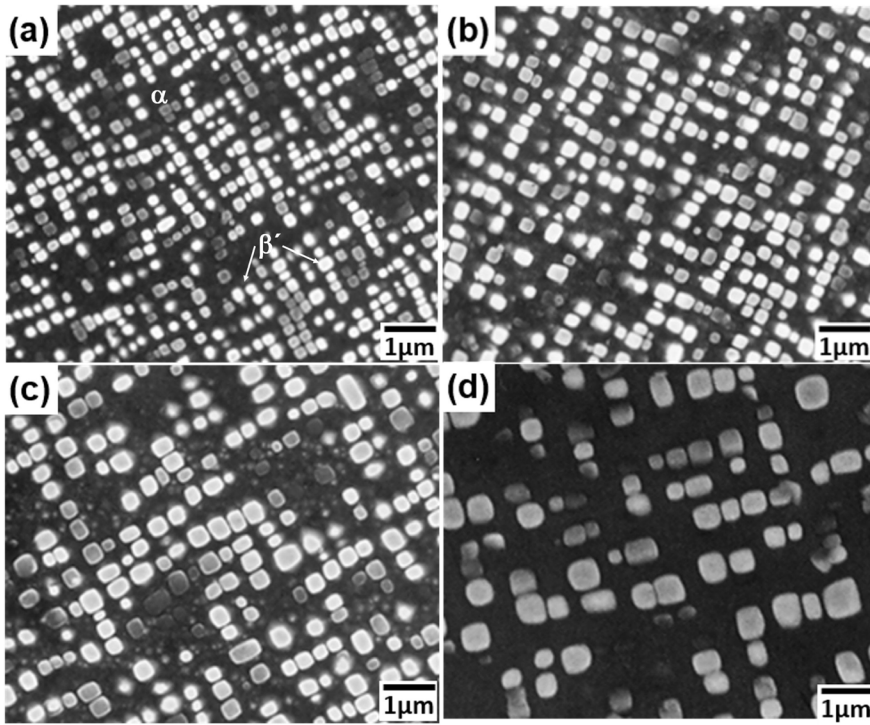


**Figure 6.** FEG-SEM micrographs of the precipitation evolution for the Fe-10at.%Ni-15at.%Al alloy aged at 850 °C for (a) 10, (b) 25, (c) 50 and (d) 100 h.

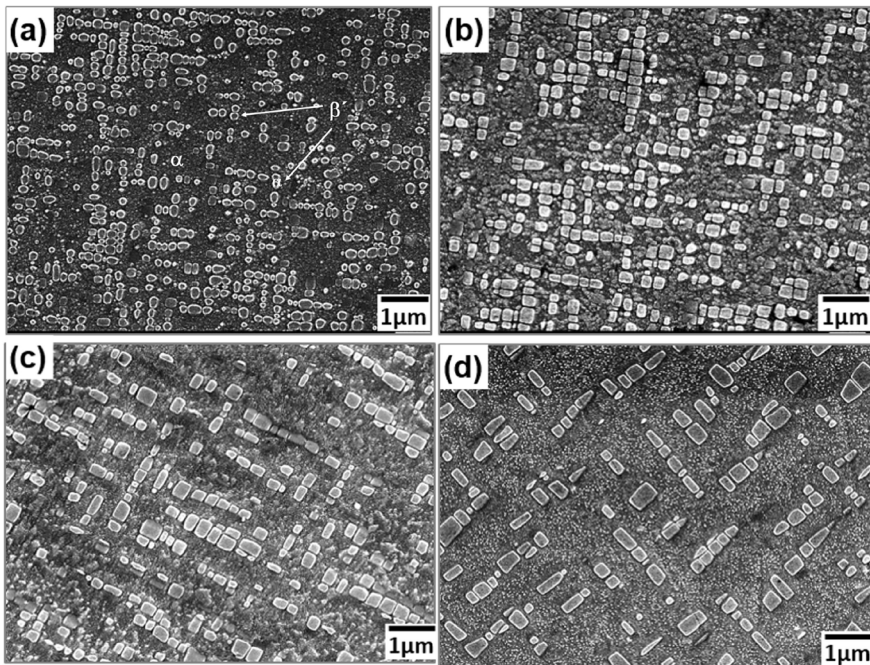


**Figure 7.** FEG-SEM micrographs of the precipitation evolution for the Fe-10at.%Ni-15at.%-2.5at.%CuAl alloy aged at 850 °C for (a) 10, (b) 25, (c) 50 and (d) 100 h.

Fe-10at.%Ni-15at.%Al alloy, the shape of  $\beta'$  precipitates is spheroid at the early times of aging, which can be attributed to the fact that the interfacial free energy  $\gamma$  between the matrix and precipitate is more predominant than that of the elastic-

strain energy<sup>24</sup>, and the sphere shape minimizes the interfacial energy. As the aging at 850 °C of this alloy progresses, the precipitate morphology changes to cuboids, Figure 6a, because the effect of elastic-strain energy on the morphology

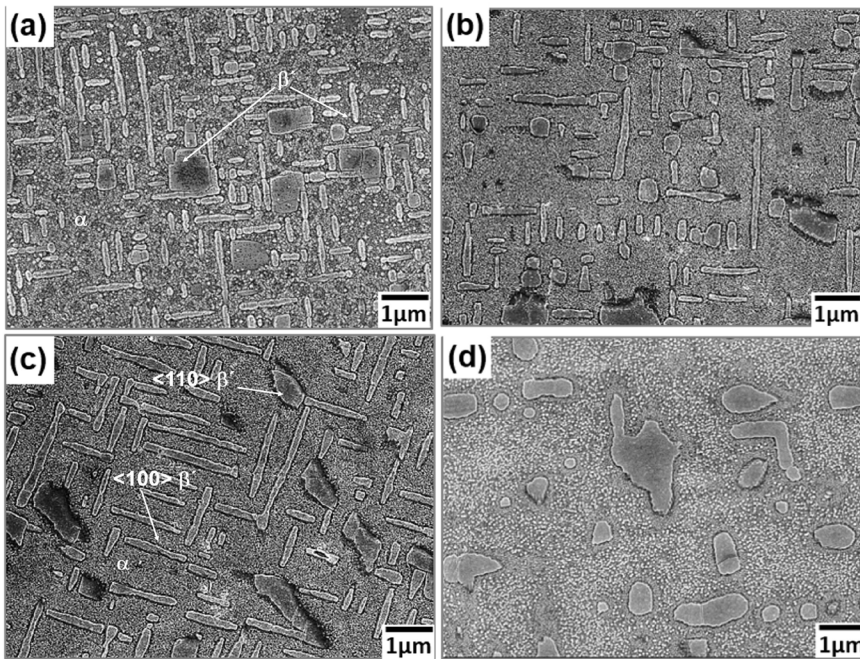


**Figure 8.** FEG-SEM micrographs of the precipitation evolution for the Fe-10at.%Ni-15at.%-5at.%CuAl alloy aged at 850 °C for (a) 10, (b) 25, (c) 50 and (d) 100 h.

is more significant than that of the interfacial energy<sup>25</sup>, and the cuboid shape produces a higher decrease of free energy<sup>24</sup>. The presence of straight sides for the cuboid precipitates suggests the existence of a coherent interface between the precipitate and the matrix and thus, the elastic-strain energy seems to become dominant<sup>7,25</sup>. The  $\beta'$  precipitates turn out to be aligned with the ferrite matrix over with aging time, Figure 6b and c. Further aging promotes the coarsening process of precipitates, Figure 6c and d. Aging for longer times shows the formation of square or rectangular arrays of cuboid precipitates, Figure 6d, and then they are expected to coalesce and form plates for longer aging times<sup>14,15</sup>. That is, this alignment is promoted to overcome the elastic-strain energy originated by the increase in the volume of these coherent precipitates during its coarsening<sup>25</sup>. The volume fraction of  $\beta'$  precipitates was determined to be about 0.1 for this alloy, aged at 850 °C, which shows a good agreement with 0.095 determined by Thermo-Calc, Figure 2a.

In the case of the aging at 850 °C for the 2.5 at.%Cu containing alloy, the precipitation evolution takes place slightly slower, Figure 7a-d, than that previously described. That is, the morphology of  $\beta'$  phase is round and irregular for times of 10 h, Figure 7a. Then the shape of  $\beta'$  precipitates becomes like cuboids as the aging progresses, Figure 7b. The array of  $\langle 100 \rangle$  aligned cuboid  $\beta'$  precipitates can be observed for this alloy aged for 50 h, Figure 7c. These arrays originate a plate morphology of  $\beta'$  precipitates for the alloy aged for 100 h, Figure 7d. In contrast, the aging of 5 at. % Cu-containing alloy indicates the presence of  $\langle 100 \rangle$  elongated plate  $\beta'$  precipitates, Figure 8b. These plate precipitates coarsen very quickly, Figure 8b. The morphology of coarsened  $\beta'$  precipitates changes to irregular with a preferential alignment along the  $\langle 110 \rangle$  crystallographic direction, Figure 8c,

which is the elastically softest direction of the bcc ferrite matrix<sup>14-17</sup>. The alignment of  $\langle 110 \rangle \beta'$  precipitates was determined considering that these precipitates are at 45° from those with  $\langle 100 \rangle$  alignment, defined using Figure 5. These irregular and incoherent precipitates coarsen very fast. Fine precipitation of  $\beta'$  cuboids can be observed in this micrograph because of the air-cooling after aging. It is important to note that the morphology of  $\beta'$  precipitates is quite different for this composition from those observed for the other compositions. This is attributable to the highest interfacial energy promoted by the Cu content, as explained in the next section.

The volume fraction of  $\beta'$  precipitates was determined to be 0.15 and 0.17 for the 2.5at.%Cu and 5 at. % Cu-containing alloys, respectively, aged at 850 °C for 100 h. These values are consistent with the Calphad calculated ones, 0.134 and 0.177 for the 2.5 at.%Cu and 5 at. % Cu-containing alloys, respectively, as shown in Figure 2b and c.

Figure 9a-e illustrates, for example, the EDX FEG-SEM Fe, Ni, Al and Cu elemental mapping for the Fe-10at.%Ni-15at.%Al-2.5at.%Cu alloy aged at 850 °C for 100 h. These images suggest that the Fe is mainly located in the  $\alpha$  ferrite phase, Ni, Al and Cu are distributed in the  $\beta'$  precipitates, which shows a good agreement with the Calphad calculated results, as shown in Figures 3 and 4b and c. In order to compare the chemical composition of the  $\langle 100 \rangle$  direction-aligned  $\beta'$  precipitates with that of  $\langle 110 \rangle$  direction-aligned ones, Table 1 shows the EDX FEG-SEM point analysis of these precipitates. It can be noted that the chemical composition is very similar for both  $\langle 100 \rangle$ -aligned and  $\langle 110 \rangle$ -aligned  $\beta'$  precipitates. As shown in Figure 3b and c, these results are in good agreement with Calphad results. Table 1 also verifies that no fcc Cu precipitation occurred

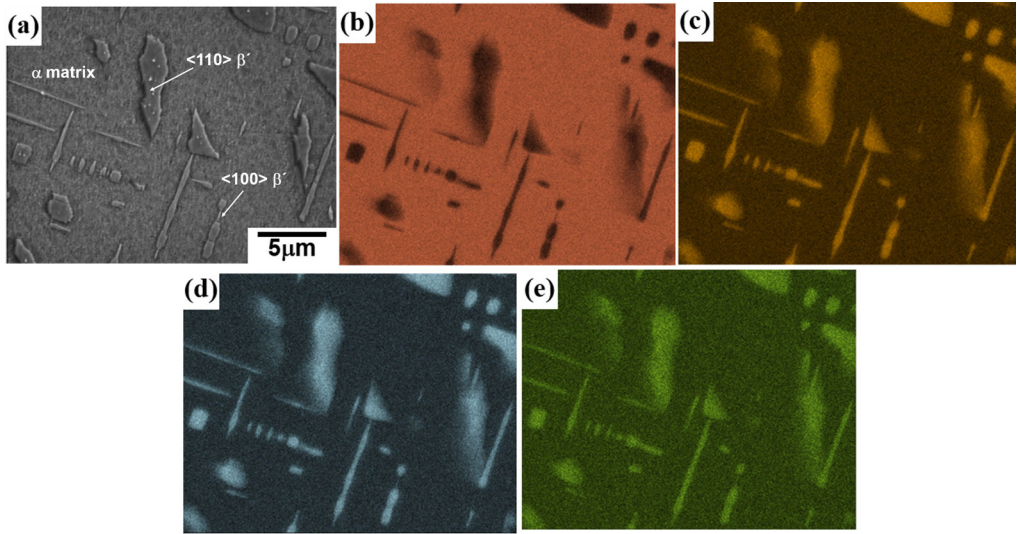


**Figure 9.** (a) FEG-SEM image and the corresponding EDX-SEM elemental mapping images of (b) Cr, (c) Mn, (d) Ni, and (e) Fe for the Fe-10at.%Ni-15at.%Al-5at.%Cu alloy aged at 850 °C for 100 h.

**Table 1.** EDX-SEM analysis of  $\beta'$  precipitates for the Fe-10at.%Ni-15at.%Al-5at.%Cu alloy aged at 850 °C for 100 h.

Alignment	at. % Fe	at. % Ni	at. % Al	at. % Cu
<100>	17.0±0.26	30.0±0.26	40.0±0.90	13.0±0.90
<110>	18.0±0.23	29.0±0.43	44.0±0.86	9.0±0.67

during the aging treatment of the Cu-containing alloys. This fact is thermodynamically predicted from Figure 2c. That is, the fcc Cu precipitation is only possible for aging temperatures lower than approximately 600 °C.

### 4.3. Precipitation of growth kinetics

The growth kinetics of precipitation was analyzed using the Precipitation/Kinetics software. For instance, Figure 10a-c show the calculated variation of mean radius  $r$  as a function of time  $t$ , as indicated by the continuous line. Additionally, the experimental values of equivalent radius  $r$  are also included in this figure, as shown by the triangle marks. The calculated curve of Figure 10a-c shows slow growth kinetics of precipitate radius with time for short times, which can be associated with the nucleation stage. Then, the growth kinetics is accelerated because of the nucleation and growth stage. To continue, the growth kinetics is slightly decelerated, and it corresponds to the coarsening stage of precipitates<sup>20,21</sup>. The experimental radius values of this work alloys are in the coarsening stage. This fact was confirmed following the variation of equivalent radius  $r$  as a function of aging time  $t$ . This growth kinetics usually obeys a power law,  $r = kt^n$ , and the time exponent  $n$  usually indicates the coarsening mechanism. The time exponent values  $n$  were determined to be about 0.27-0.30 for all aged alloy compositions, as shown in Table 2, which indicate a diffusion-controlled coarsening process, according to the Lifshitz-Slyozov-Wagner LSW theory<sup>25</sup>. Besides, the position of Precipitation/Kinetics software calculated growth kinetics curve of Figure 10a-c can be modified by selecting a value of the free interfacial energy  $\gamma$ . Figure 10a-c also present the value of  $\gamma$ , which gives the best fit between the calculated

**Table 2.** Experimental values of  $\gamma$ , and  $k$  and  $n$  constants for present work alloys.

at. % Cu	Experimental $\gamma$ (J m <sup>-2</sup> )	Experimental $k$ (m <sup>3</sup> s <sup>-1</sup> )	Time exponent $n$
0	0.01	0.3330 x10 <sup>-25</sup>	0.27
2.5	0.009	0.1432x10 <sup>-25</sup>	0.26
5.0	0.040	1.0630x10 <sup>-25</sup>	0.30

curve and the experimental values. It is essential to mention that the calculation of Precipitation/Kinetics software follows the LSW theory for diffusion-controlled coarsening. This behavior implies low volume fraction of sphere precipitates and elastic-strain between the matrix and precipitates, and solute-rich precipitates<sup>25</sup>, which is not the case for the Fe-Ni-Al and Fe-Ni-Al-Cu alloys. Thus, the determination of interfacial energy  $\gamma$  is not accurate; however, the energy values could be used to explain the coarsening behavior of the present work alloys qualitatively. Table 2 presents the experimental  $\gamma$  values, the coarsening constant  $k$ , and time exponent  $n$  for the present work alloys. These values of  $k$  and  $n$  are in good agreement with those reported in the literature<sup>14,15,17</sup>. The coarsening behavior,  $k$  coarsening constant, can be explained according to the interfacial free energy  $\gamma$ . That is, the decrease in the coarsening constant  $k$  during aging of the 2.5 at. %-containing alloy, as shown in Table 2, seems to be related to the decrease in the interfacial free energy  $\gamma$ , since the constant  $k$  is directly proportional to the interfacial energy. Additionally, the Cu atomic diffusion is expected to decrease because of the low solubility in the ferrite matrix phase, which may also favor a higher coarsening resistance of this alloy. In contrast, the

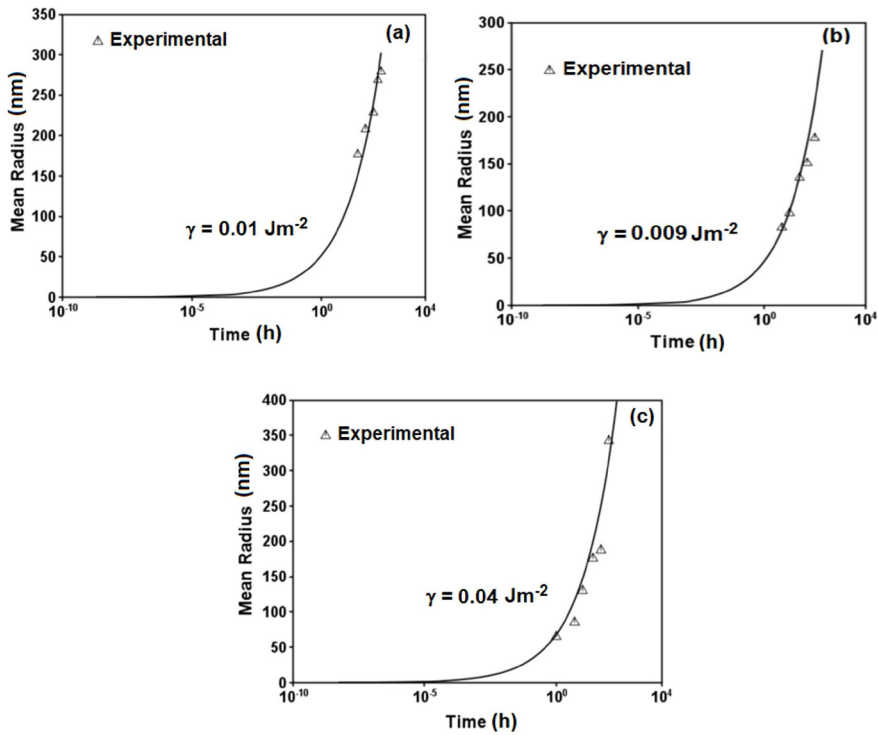


**Figure 10.** Precipitation/Kinetic software calculated curve and experimental values of average radius vs. time for the (a) Fe-10at.%Ni-15at.%Al, (b) Fe-10at.%Ni-15at.%Al-2.5at.%Cu and (c) Fe-10at.%Ni-15at.%Al-5at.%Cu alloys aged at 850 °C.

5 at% Cu content caused the highest coarsening constant  $k$ , which is attributable to the highest interfacial free energy  $\gamma$ , as shown in Table 2. Furthermore, an interfacial energy value of 0.04 J/m<sup>2</sup> may indicate that the interface between the  $\beta'$  precipitate and the ferritic phase could be semicoherent or incoherent, as suggested by the irregular morphology of  $\beta'$  precipitates, Figure 8d. Conversely, a value of 0.01 or 0.009 J/m<sup>2</sup> corresponds to a coherent interface between the precipitate and the matrix<sup>25</sup>, showing a planar interface between them, Figures 6 and 7a-d. The high interfacial free energy can also be adopted as the reason for the  $\langle 110 \rangle$  alignment of  $\beta'$  precipitates to reduce the total free energy of the system.

The Precipitation/Kinetics software calculated the chemical composition of the ferritic matrix and  $\beta'$  precipitates as a function of aging time is shown in Figures 11 and 12a-c, respectively, for the present work alloys.

The matrix supersaturation is about 15 at.% Al and 10 at.% Ni for all the alloys, the composition balance is Fe. As the aging progresses, the Al and Ni contents diminish to approximately 13 and 7 at.%, respectively, and then it remains almost constant. The Cu content also shows a decrease to about 1.7 and 2.1 at.% Cu for the 2.5 and 5 at.% Cu-containing alloys, respectively. In contrast, the chemical composition of  $\beta'$  precipitates shows interesting behavior. That is, The Ni content is slightly higher than that of Al for the aged Fe-10at.%Ni-15at.%Al alloy; however, this difference becomes smaller for the aged Fe-10at.%Ni-15at.%Al-2.5at.%Cu alloy. That is, the atomic relation of Ni to Al is almost one to one, close to NiAl intermetallic compound. Furthermore, the difference is reversed for the aged Fe-10at.%Ni-15at.%Al-5at.%Cu alloy. That is, the Al content

is higher than that of Ni. This behavior may also be adopted as the reason for the fastest coarsening process of the  $\beta'$  precipitate because of the faster atomic diffusion process in this case<sup>24</sup>. The Precipitation/Kinetics software results also show that the precipitation growth kinetics is the fastest for the ternary alloy, while the slowest kinetics correspond to the 5 at.%Cu-containing alloy, which may be attributed to the highest interfacial energy  $\gamma$ <sup>24</sup>.

#### 4.4. Response to aging treatment

The plot of Vickers hardness versus aging time, aging curve, is shown in Figure 13 for the Fe-10at.%Ni-15at.%Al, 10at.%Ni-15at.%Al-2.5at.%Cu and Fe-10at.%Ni-15at.%Al-5at.%Cu alloys aged at 850 °C. The hardness of the solution treated Cu-containing alloys is about 420 VHN, which is lower than that reported for the ternary alloy, 438 VHN. This behavior may be attributed to the low Cu solid solution strengthening because of the formation of Cu cluster during air-cooling after solution treatment<sup>24</sup>, as shown in Figure 1. The volume fraction of precipitated fcc Cu is very low, less than 1 vol.% according to Calphad calculation, in the solution treatment. Thus, the contribution of fcc Cu precipitates is meager to be taken into account. An increase in hardness,  $\Delta H_V$ , between 50 and 70 VHN, was determined for the two Cu-containing alloys in comparison to that of the solution treated specimen, as a result of the  $\beta'$  precipitation process at 850 °C. No precipitation of fcc Cu is thermodynamically possible at this aging temperature, Figures 1 and 2c. This increase is higher than that of the ternary alloy,  $\Delta H_V = 45$  VHN at 850 °C. The highest aging response of Cu-containing alloys can be attributable to the fact that the Cu addition

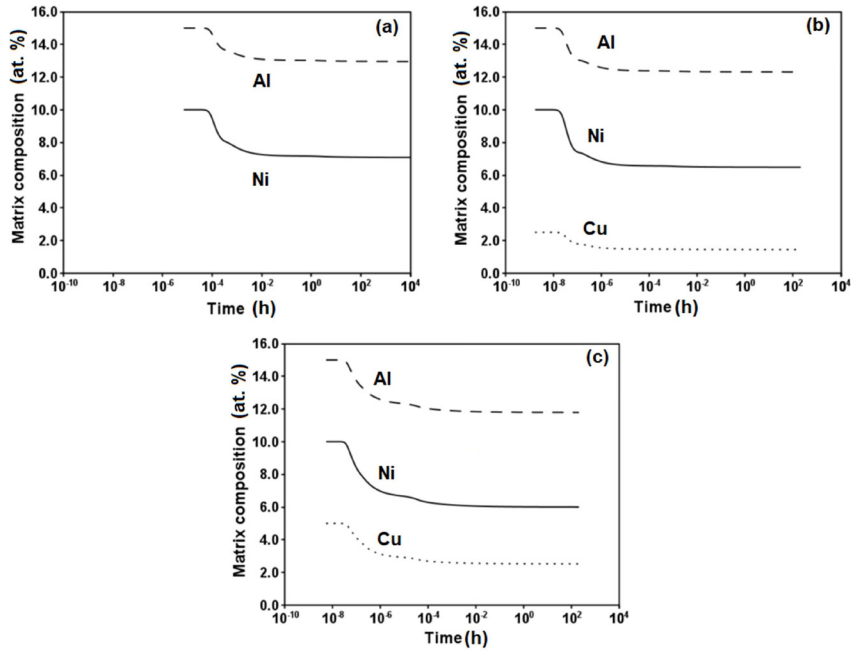


**Figure 11.** Precipitation/Kinetic software calculated chemical composition of ferritic matrix vs. time for the (a) Fe-10at.%Ni-15at.%Al, (b) Fe-10at.%Ni-15at.%Al-2.5at.%Cu and (c) Fe-10at.%Ni-15at.%Al-5at.%Cu alloys aged at 850 °C.

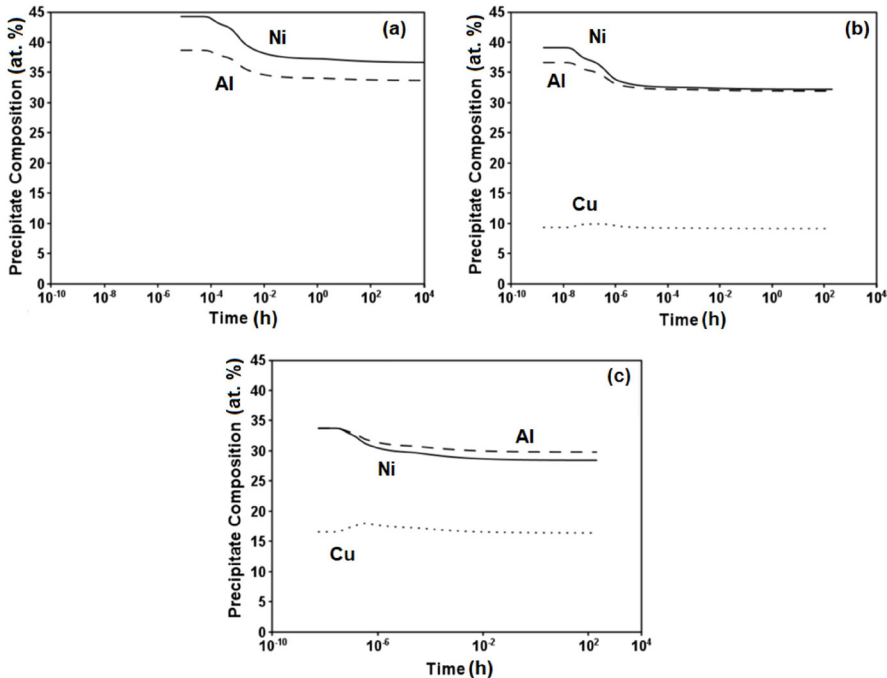


**Figure 12.** Precipitation/Kinetic software calculated chemical composition of  $\beta'$  precipitates vs. time for the (a) Fe-10at.%Ni-15at.%Al, (b) Fe-10at.%Ni-15at.%Al-2.5at.%Cu and (c) Fe-10at.%Ni-15at.%Al-5at.%Cu alloys aged at 850 °C.

increases the volume fraction of the  $\beta'$  precipitates, as shown in Figure 2b and c, and it promotes the increase in Cu content of the  $\beta'$  precipitates, as shown in Figure 4b and c. That is, it decreases the iron content of the  $\beta'$  precipitates, and its chemical composition is closer to the composition of NiAl intermetallic. The aging curves at 850 °C for the ternary

and 5at.%Cu-containing alloy have a similar hardening behavior. That is, both curves show an increasing tendency for hardness, while the 2.5 at. % Cu-containing alloy shows an aging curve with a clear hardness peak, followed by an overaging stage, and subsequently, the hardness remains almost constant.

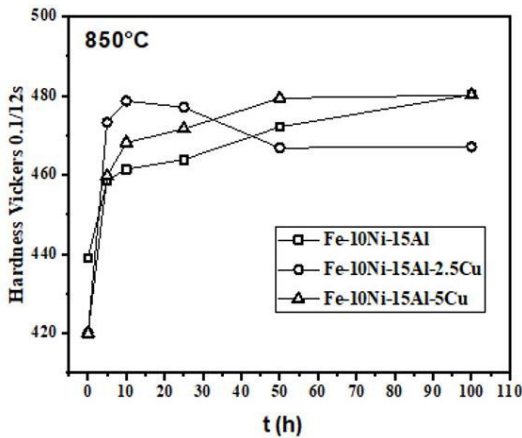


**Figure 13.** Aging curves for the Fe-10at.%Ni-15at.%Al, Fe-10at.%Ni-15at.%Al-2.5at.%Cu and Fe-10at.%Ni-15at.%Al-5at.%Cu alloys aged at 850 °C.

## 5. Conclusions

Numerical and experimental analyses of the growth kinetics of precipitation and coarsening processes were carried out during the isothermal aging at 850 °C for Fe-10at.%Ni-15at.%Al, Fe-10at.%Ni-15at.%Al-2.5at.%Cu and Fe-10at.%Ni-15at.%Al-5at.%Cu alloys, and the conclusions are as follows:

1. Calphad calculated results indicated that the Cu addition promoted a higher volume fraction of  $\beta'$  precipitates than that of the ternary alloy, and the Fe content in precipitates is also reduced. The Cu alloying element is mainly located in the  $\beta'$  precipitate.
2. A content of 2.5 at. % Cu decreased the interfacial free energy  $\gamma$  between the  $\beta'$  precipitate and the ferritic matrix, and it caused a lower coarsening constant  $k$  than that of the ternary alloy. In contrast, the interfacial free energy increased considerably for the 5 at. % Cu-containing alloy, which caused the fastest coarsening kinetics and an irregular morphology of precipitates aligned in the  $\langle 110 \rangle$  crystallographic direction of the ferrite phase. This fact suggests that the addition of a Cu content lower than 2.5 at. % could be beneficial to improve the coarsening resistance.
3. The aging response of Cu-containing alloys was higher than that of the ternary alloy because of the higher volume fraction of  $\beta'$  precipitates, and its chemical composition close to the NiAl intermetallic compound.
4. The above results suggest that the addition of a Cu content lower than 2.5 at. % to Fe-Ni-Al alloys could be beneficial to improve the coarsening resistance and mechanical strength at high temperature.

## 6. Acknowledgements

The authors wish to acknowledge financial support from SIP-IPN and Conacyt A1-S-9682.

## 7. References

1. Guo Z, Sha W, Vaumosse D. Microstructural evolution in a PH13-8 stainless steel after ageing. *Acta Mater.* 2003;51:101-16.
2. Stallybrass C, Sauthoff G. Ferritic Fe-Al-Ni-Cr alloys with coherent precipitates for high-temperature applications. *Mater Sci Eng A.* 2004;387:985-90.
3. Stallybrass C, Schneider A, Sauthoff G. The strengthening effect of (Ni,Fe)Al precipitates on the mechanical properties at high temperatures of ferritic Fe-Al-Ni-Cr alloys. *Intermetall.* 2005;13:1263-8.
4. Rawlings MJS, Liebscher CH, Asta M, Dunand DC. Effect of titanium additions upon microstructure and properties of precipitation-strengthened Fe-Ni-Al-Cr ferritic alloys. *Acta Mater.* 2017;128:103-12.
5. Sun Z, Liebscher CH, Huang S, Teng Z, Song G, Wang G, et al. New design aspects of creep-resistant NiAl-strengthened ferritic alloys. *Scr Mater.* 2013;68:384-8.
6. Muñoz-Morris MA, Morris DG. Microstructure and mechanical behavior of a Fe-Ni-Al alloy. *Mater Sci Eng A.* 2007;444:236-41.
7. Baldan A. Progress in Ostwald ripening theories and their applications to nickel-base superalloys. *J Mater Sci.* 2002;37:2171-202.
8. Kuchmann CJ, Voorhees PW. Ostwald ripening in ternary alloys. *Metall Mater Trans, A Phys Metall Mater Sci.* 1996;27:937-43.
9. Lifshitz IM, Slyozov VV. The kinetics of precipitation from supersaturated solid solution. *Phys Chem Solids.* 1961;19:35-50.
10. Wagner C. Theorie der alterung von niederschlagen durch umlosen. *Z. Electrochem.* 1961;65:581-91.
11. Ges A, Fornaro O, Palacio H. Long term coarsening of  $\gamma'$  precipitates in a Ni-base superalloy. *J Mater Sci.* 1997;32:3687-91.
12. Thornton K, Akaiwa N, Voorhees PW. Large-scale simulations of Ostwald ripening in elastically stressed solids: I. Development of microstructure. *Acta Mater.* 2004;52:1365-78.
13. Ardell AJ. The effect of volume fraction on particle coarsening: theoretical considerations. *Acta Metall.* 1972;20:61-71.
14. Rosales-Dorantes HJ, Cayetano-Castro N, Lopez-Hirata VM, Saucedo Muñoz ML, Villegas-Cardenas JD, Hernández-Santiago F. Coarsening process of coherent  $\beta'$  precipitates in Fe-10 wt-%Ni-15 wt-%Al and Fe-10 wt-%Ni-15 wt-%Al-1 wt-%Cu alloys. *Mater Sci Technol.* 2013;29:1492-8.
15. Cayetano-Castro N, Saucedo-Muñoz ML, Dorantes-Rosales HJ, Gonzalez-Velazquez JL, Villegas-Cardenas JD, Lopez-Hirata VM. Ostwald ripening process of coherent  $\beta'$  precipitates during aging in  $Fe_{0.75}Ni_{10.0}Al_{0.15}$  and  $Fe_{0.74}Ni_{10.10}Al_{0.15}Cr_{0.01}$  alloys. *Adv Mater Sci Eng.* 2014;5:485626.
16. Kapoor M, Isheim D, Ghosh G, Vaynman S, Fine ME, Chung Y. Aging characteristics and mechanical properties of 1600 MPa body-centered cubic Cu and B2-NiAl precipitation-strengthened ferritic steel. *Acta Mater.* 2014;73:56-74.
17. Ferreira-Palma C, Contreras-Piedras E, Cayetano-Castro N, Saucedo-Muñoz ML, Lopez Hirata VM, Gonzalez-Velazquez JL, et al. Effect of temperature and composition on NiAl precipitation and morphology in Fe-Ni-Al alloys. *Metall Mater Trans, A Phys Metall Mater Sci.* 2017;48:5285-93.
18. Saucedo-Muñoz ML, Ortiz-Mariscal A, Lopez-Hirata VM, J Villegas-Cardenas JD, Soriano-Vargas O, Avila-Davila EO. Precipitation analysis of as-cast HK40 steel after isothermal aging. *Int J Miner Metall Mater.* 2017;24:1125-33.
19. Cueto-Rodriguez MM, Avila-Davila EO, Lopez-Hirata VM, Saucedo-Muñoz ML, Palacios-Pineda LM, Trapaga-Martinez LG, et al. Numerical and experimental analyses of the effect of heat treatments on the phase stability of Inconel 792. *Adv Mater Sci Eng.* 2018;2018:1-7.
20. Lopez-Hirata VM, Hernandez-Santiago F, Saucedo-Muñoz ML, Dorantes-Rosales HJ, Paniagua-Mercado AM. Analysis of  $\beta'$ (Cu4Ti) Precipitation during isothermal aging of a Cu-4wt.%Ti alloy. *Mater Res.* 2018;21:e20180121.
21. Thermo-Calc software. TCFE9.tdb and MobFe5 data. Version 2021a. Sweden: Thermo-Calc software; 2021.

22. Janssens KGF, Raabe D, Kozeschnik E, Miodownik MA, Nestler B. Computational materials engineering. London: Academic Press; 2007.
23. Handbook ASM. Alloy phase diagrams. Vol. 3. Ohio: ASM International; 1992.
24. Heo Y-U, Kim Y-K, Kim J-S, Kim J-K. Phase transformation of Cu precipitates from bcc to fcc in Fe-3Si-2Cu alloy. Acta Mater. 2013;61:519-28.
25. Kostorz G. Phase transformations in materials. Germany: Wiley-VCH; 2001.